High energy density asymmetric pseudocapacitors fabricated by graphene/carbon nanotube/MnO$_2$ plus carbon nanotubes nanocomposites electrode

Chung Jung Hung [a], Pang Lin [a], Tseung Yuen Tseng [b],*

[a] Department of Materials Science and Engineering, National Chiao Tung University, Hsinchu 300, Taiwan
[b] Department of Electronics Engineering and Institute of Electronics, National Chiao Tung University, Hsinchu 300, Taiwan

HIGHLIGHTS

- The nanocomposite electrode achieves the specific capacitance of 964 F g^{-1} at 1 A g^{-1}.
- The asymmetric pseudocapacitor possesses energy density of record high 304 Wh kg^{-1}.
- The asymmetric pseudocapacitor shows excellent cycling stability.

ARTICLE INFO

ABSTRACT

Novel graphene/carbon nanotubes (CNTs)/manganese oxide (MnO$_2$) nanocomposites plus CNTs (GMC + C) and graphene/CNTs hybrid (GC) thin-film electrodes are prepared by electrophoretic deposition (EPD). These nanocomposite electrodes exhibit high surface area and interconnected pore networks. The GMC + C nanocomposite electrode shows excellent specific capacitance of 964 F g^{-1} at 1 A g^{-1}, rate capability with the residual capacitance of 529 F g^{-1} at 500 mV s^{-1}, and fast Na$^+$ diffusion with intercalation value of 6.34 × 10^{-7} cm^2 s^{-1}, and deintercalation value of 8.86 × 10^{-7} cm^2 s^{-1}. Such excellent pseudocapacitive performances are attributed to low ion/electron transport resistances and short ion/electron diffusion lengths. Furthermore, novel aqueous electrolyte-based asymmetric pseudocapacitor having 1.8 V cell voltage is successfully fabricated using GMC + C nanocomposite as a cathode and GC nanocomposite as an anode. The optimized asymmetric pseudocapacitor possesses superior performance with a maximum energy density of record high 304 Wh kg^{-1} and retaining 56.2% of its initial specific energy density at the power density up to 242 kW kg^{-1}. In addition, the asymmetric cell configuration also shows excellent cycling stability with 89% specific capacitance maintained after 10,000 cycles. These results suggest that our designed asymmetric pseudocapacitors have a high potential for practical applications.

1. Introduction

To achieve high power and long life cycle devices than batteries, electrochemical capacitors or supercapacitors (SCs) attracts much more attention for future energy storage applications. In terms of charge storage mechanisms, SCs are mainly classified into electrical double-layer capacitors (EDLCs) and pseudocapacitors [1,2]. In general, EDLCs have high power density and long life cycle but suffer from relatively low energy density; however, pseudocapacitors exhibit higher specific capacitance and energy density than EDLCs, but poor cycle ability. In other words, their limitation is that the energy density value of SCs is still far below that battery, which has restricted their potential applications [3—5]. Hence, it is crucial to increase the energy density of SCs to meet the future energy demands without sacrificing excellent power density.

Technically, the effective way to improve the energy density for SCs depends on enhancing the intrinsic capacitance of active materials or increasing the operating voltage of the system [6]. Conventionally, many of the envisioned applications have emerged in the replacement of aqueous electrolyte with organic electrolytes or ionic liquids to offer better electrochemical stability and extend the cell potential window, which result in a higher energy density

than aqueous electrolytes [7–9]. However, these non-aqueous electrolytes are generally more expensive and not eco-friendly in comparison to aqueous electrolytes. In addition, non-aqueous SCs usually exhibit low capacitive and power capabilities, attributing to low ionic conductivity and higher specific resistance, which limit the cell performance [10].

In other words, using SCs based on aqueous electrolytes have excellent ion conductivity to minimize the internal resistance leading to faster charging/discharging properties. In particular, they also offer advantages of low-cost green manufacturing and enhanced safety in operation, which make these aqueous electrolytes becoming a very attractive for electrochemical capacitors [11]. However, it is well-known that aqueous electrolytes limit the individual SCs cell voltage to roughly 1.2 V (theoretical decomposition voltage of water, 1.23 V).

In order to extend the operating voltage, much research effort has been focused on asymmetric pseudocapacitors for a two-electrode setup working in well-separated potential windows in the same electrolyte [12–17]. It is anticipated that, this designed asymmetric two-electrode configuration operating in neutral electrolytes can bring both the EDLC (anode, as the power source) and pseudocapacitive (cathode, as the energy source) behavior together, leading to increase operating voltage and thus significantly improve the energy density while retaining their intrinsic high specific power [18–21].

We previously reported that hybrid graphene/MnO_2/CNTs ternary nanocomposites films were directly deposited on a nickel plate collector as high performance electrodes of pseudocapacitor via EPD method without adding any binder or surfactants during processing [22,23]. Moreover, EPD, in contrast to other processing methods, offers several significant advantages such as low cost, rapid fabrication, non-vacuum approach, room-temperature processing, eco-friendly, additive free, scalable and suitability for mass production. In addition, it can also control the mass of the deposited particles, namely, thickness of the films can be easily controlled by the concentration of the suspension, applied potential, and deposition time. Regarding the engineering feasibility study, EPD method is the most feasible option for the practical application of pseudocapacitor.

As far as our knowledge, there are only a very few reports explored the fabrication of hybrid nanocomposites thin-film electrode for asymmetric pseudocapacitors cell assemblies by EPD method. We used EPD method to fabricate novel hybrid functional nanocomposite electrodes for asymmetric pseudocapacitors with improved electrochemical properties, such as achieving high energy density, high power density and long cycle lifetime. Herein, we report a straightforward approach to fabricate an aqueous electrolyte-based asymmetric pseudocapacitors based on a designed GMC + C ternary nanocomposite cathode, and a GC binary nanocomposite anode. Combining the unique properties of each functional material, the present strategy employs hybrid nanocomposite thin-film electrodes with porous network structure, which makes the SCs exhibiting excellent power capability and lower equivalent series resistance.

2. Experimental

Designed hybrid GMC + C and GC nanocomposites as asymmetric pseudocapacitor electrode materials were directly deposited onto 10 mm × 30 mm × 1 mm flat Ni substrates by EPD method. Before electrophoresis, Ni substrate was etched with 10% nitric acid solution for 30 min to obtain rough surface and thoroughly cleaned with deionized (DI) water in an ultrasonic bath, and dried in an oven at 100 °C for 12 h. The commercial CNTs (specific surface area: 40–300 m^2 g^{-1}, length: 5–20 μm) was purified by boiling at 70%

nitric acid solution for 24 h, followed by rinsed with DI water and dried in an oven at 100 °C for 12 h before synthesizing nanocomposites.

2.1. Synthesis of graphene

Graphene was prepared by reducing the graphene oxide synthesized by chemical oxidation and exfoliation of natural graphite fine powder using a modified experiment by Rakhi et al. [24]. In a typical synthesis, we first employed the modified Hummers methods to prepare graphene oxide. The detailed synthesis procedure is reported elsewhere [23]. 100 mg of graphene oxide was dispersed in 50 mL DI water having 30 min ultrasonic agitation, to achieve brown color suspension. Subsequently, graphene oxide suspension was reacted with a given amount of sodium hydroxide (NaOH) (pH = 14.0) in a water bath at 95 °C for 12 h, the brown color suspension now turned into completely black. After the suspension cooled down to room temperature, the as-synthesized product of the reacting suspension was collected and then centrifuged followed by thoroughly rinsed with DI water. Finally, the obtained product, graphene was dried in air at 110 °C for overnight followed by a 750 °C thermal annealing under a H_2/Ar mixed gas for 30 min.

2.2. Preparation of GMC + C cathode and GC anode nanocomposites

Pseudocapacitor cathode electrode material, GMC + C nanocomposites were synthesized by using the combination of redox titration reaction and EPD technique. GMC + C nanocomposites were formed from the mixtures of graphene/MnO_2/CNTs nanocomposites and purified CNTs. Details of the apparatus and experimental procedures were described elsewhere [23]. The electrolyte used in EPD was a mixture of 0.095 g graphene/MnO_2/CNTs nanocomposites, 0.005 g CNTs powders (5 wt%), and hydrochloric acid (37%, 0.2 mL) in the isopropyl alcohol (80 mL). Powders were dispersed well in the solution using ultrasonic agitation for 30 min. The GMC + C nanocomposites were deposited using an EPD procedure. Nickel and platinum foils were dipped in this solution as cathode and anode, respectively at a distance of 1 cm. The nanocomposite powders were electrophoretically deposited on Ni substrate at a 50 V direct current (DC) voltage for 2 min. After EPD, the GMC + C nanocomposite film formed on Ni substrate (as-grown nanocomposites electrode) was dried in an oven at 110 °C for 12 h.

Pseudocapacitor anode electrode material, GC nanocomposite was synthesized by using the same technique. Briefly, purified CNTs (0.05 g) were dispersed in the mixture solution of hydrochloric acid (37%, 0.2 mL) and isopropyl alcohol (80 mL) with as-synthesized graphene (0.05 g), and then ultrasonicated for 30 min to produce a uniform suspension. Nickel and platinum foil were kept parallel at 1 cm apart in the suspension as cathode and anode, respectively. The EPD was carried out by applying a constant 50 V DC voltage for 1.5 min. After EPD, the GC nanocomposite film formed on Ni substrate was dried in an oven at 110 °C for 12 h.

2.3. Fabrication of asymmetric pseudocapacitor system

Asymmetric pseudocapacitor system was successfully constructed with a simple two-electrode configuration which was composed of GC anode and GMC + C cathode. Here, the anode and cathode were assembled with a separator (DuPont™ Nafion® NRE211 membrane) sandwiched in between. After pressing, the cathode and anode collectors were wrapped with Teflon tape and then infiltrated with 0.1 M Na_2SO_4 as the electrolyte solution, until

all air was replaced. To fabricate two-electrode asymmetric pseudocapacitor, the loading mass ratio of active materials (GMC + C/GC) was estimated to be 0.2 from the specific capacitances, calculated from the CV curves in a three-electrode cell. Its assembly consists of a cathode coated with approximately 0.55 mg GMC + C nanocomposites, and an anode coated with 2.7 mg GC nanocomposites. The mass of every as-deposited sample was measured by a high precision microbalance (PRECISA XR125SM-FR) with an accuracy of 1 μg.

2.4. Structural and properties characterization

Field emission scanning electron microscope (FE-SEM, JEOL JSM-6700) and X-ray diffractometer (XRD, Bede D1) were used to analyze surface morphology and crystallization of the film, respectively. The oxidation states of manganese oxide film were examined by X-ray photoelectron spectroscopy (XPS, ULVAC-PHI Quantera SXM). Field emission transmission electron microscope and EDS analysis (FE-TEM, JEOL JEM-2100F) were used to observe the coaxial structure of nanocomposite. The specific surface area of the nanocomposite was determined by BET (Brunauer, Emmett and Teller theory) surface area analyzer (ASAP 2020). Raman spectra of nanocomposite material were recorded using a high resolution confocal Raman microscope (HOROBA, Lab RAM HR). The laser excitation was provided by a regular model laser operating at 632.8 nm. Thermal analysis was performed from 50 to 950 °C at 3 °C min^{-1} ramping rate under air atmosphere using thermogravimetric analyzer (TGA, TA Instruments Q500).

2.5. Electrochemical testing

The electrochemical properties and specific capacitance measurements were carried out in a three-electrode cell with a saturated calomel reference electrode (SCE), platinum sheet as a counter electrode, and the prepared electrodes (GMC + C or GC nanocomposites) as a working electrode. The electrochemical characterization of asymmetric pseudocapacitors, composed of GMC + C cathode and GC anode, was carried out in a two-electrode configuration. All electrochemical measurements were carried out in a 0.1 M Na_2SO_4 solution as electrolyte. Cyclic voltammetry (CV), galvanostatic charge/discharge cycling (CC), chronoamperometry (CA) and electrochemical impedance spectroscopy (EIS) were conducted using CH Instruments 618B electrochemical analyzer at room temperature.

The specific capacitance (F g^{-1}) was calculated from CV curve using equation

$$C = \frac{\int_{E_i}^{E_f} I(E) \mathrm{d}E}{m \times v \times \left(E_f - E_i\right)} \tag{1}$$

where m is the mass of the active material, v the scan rate of CV curves (V s^{-1}), E_i the initial potential, E_f the final applied potential, and $(E_f - E_i)$ the potential window width.

The specific capacitance (F g^{-1}) from CC curve was calculated using the formula

$$C = \frac{I\Delta t}{\Delta E \times m} \tag{2}$$

where I is the discharge current, Δt the time for a full discharge, m the active material mass, and ΔE the width of the potential window for a full discharge.

3. Results and discussion

The microstructural properties of as-synthesized graphene were shown in Fig. 1. Here, we provided the modified route to synthesize graphene using a very simple refluxing process under alkaline conditions, as a replacement for highly toxic and dangerously unstable hydrazine. Under deoxygenated and heated alkaline conditions, the graphene oxide suspension was changed the color, from brown to black. Finally, graphene products were obtained by H_2/Ar gas annealing, as shown in Fig. 1a. In literature, the optical changes were observed due to the reduction of graphene oxides [25,26]. Our results demonstrate the alkaline deoxygenated treatment has the unique ability enough to remove oxygen-containing functional groups on the surface of graphene oxide, which is the evidence for reduction process.

Fig. 1b shows a surface view of as-synthesized graphene, indicating highly porous wrinkle structure. Fig. 1c illustrates the TEM image of our synthesized graphene. It can be clearly observed that as-synthesized graphene exhibits a crumpled paper-like external morphology and graphene domain area exceeds a few hundreds of square nanometers.

Fig. 1d depicts the typical nitrogen adsorption/desorption isotherm of as-synthesized graphene. The isotherm exhibits a significant hysteresis loop, indicating major nitrogen adsorption to the large porous structure. The specific surface area of as-synthesized graphene exhibits as high as 808.3 m^2 g^{-1}, and the sizes of the pores are between 34.3 and 1315.7 Å with an average pore size of 191.6 Å (as shown in the inset of Fig. 1d). Previous studies have shown that the most probable number of graphene layers could be determined according to specific surface area [27,28]. According to our experimental results, as-synthesized graphene sheets have an average thickness of approximately 1 nm, corresponding to approximately 3 stacked graphene sheets.

Raman spectroscopy has been utilized to elucidate the vibration properties of as-synthesized graphene, as shown in Fig. 1e. It can be clearly observed that there are three peaks containing 2D, G, and D bands at 2657.2, 1580.3, and 1330.4 cm^{-1}, respectively. As-synthesized graphene exhibits a weak D band which is generally considered to be the defect and disorder carbon in the graphene corresponding to the unavoidable oxidative damage during chemical exfoliation. The I_D/I_G area ratio of as-synthesized graphene is calculated to be 0.27, suggesting that the sp^2 carbon atom network becomes more and more stable within as-synthesized graphene. Nevertheless, this number is much lower than those calculated from the reduction by hydrazine [23]. In addition, the I_{2D}/I_G area ratio can be used to determine the degree of graphitization for sp^2 (C=C bonds) of graphitic materials and the number of graphene layers [29]. The I_{2D}/I_G area ratio is approximately 2.11, demonstrating that the thickness of graphene about 3–4 layers. This result is well consistent with that obtained from the BET surface area data. This result shows that the modified approach can effectively produce the graphene with less defect nature.

Designed GC and GMC + C nanocomposites are employed as electrode materials for asymmetric pseudocapacitor applications. Fig. 2a displays the morphology of GC nanocomposites electrophoretically deposited on Ni substrate, indicating that 3D hybrid carbon architecture is formed by self-assembly of the dispersions of graphene and CNT. This result implies that, it forms an open porous structure for electrolyte ions easily accessing the surface of GC.

The GMC + C nanocomposites retain porous wrinkling structure and CNTs are incorporated into the GMC + C matrix, as shown in Fig. 2b. In addition, GMC + C nanocomposites have a rough surface, which indicate the growth of MnO_2 on porous network surface. It is worth to mention that CNTs act as a bridge connecting the large graphene sheets together and filling the voids, in which such a
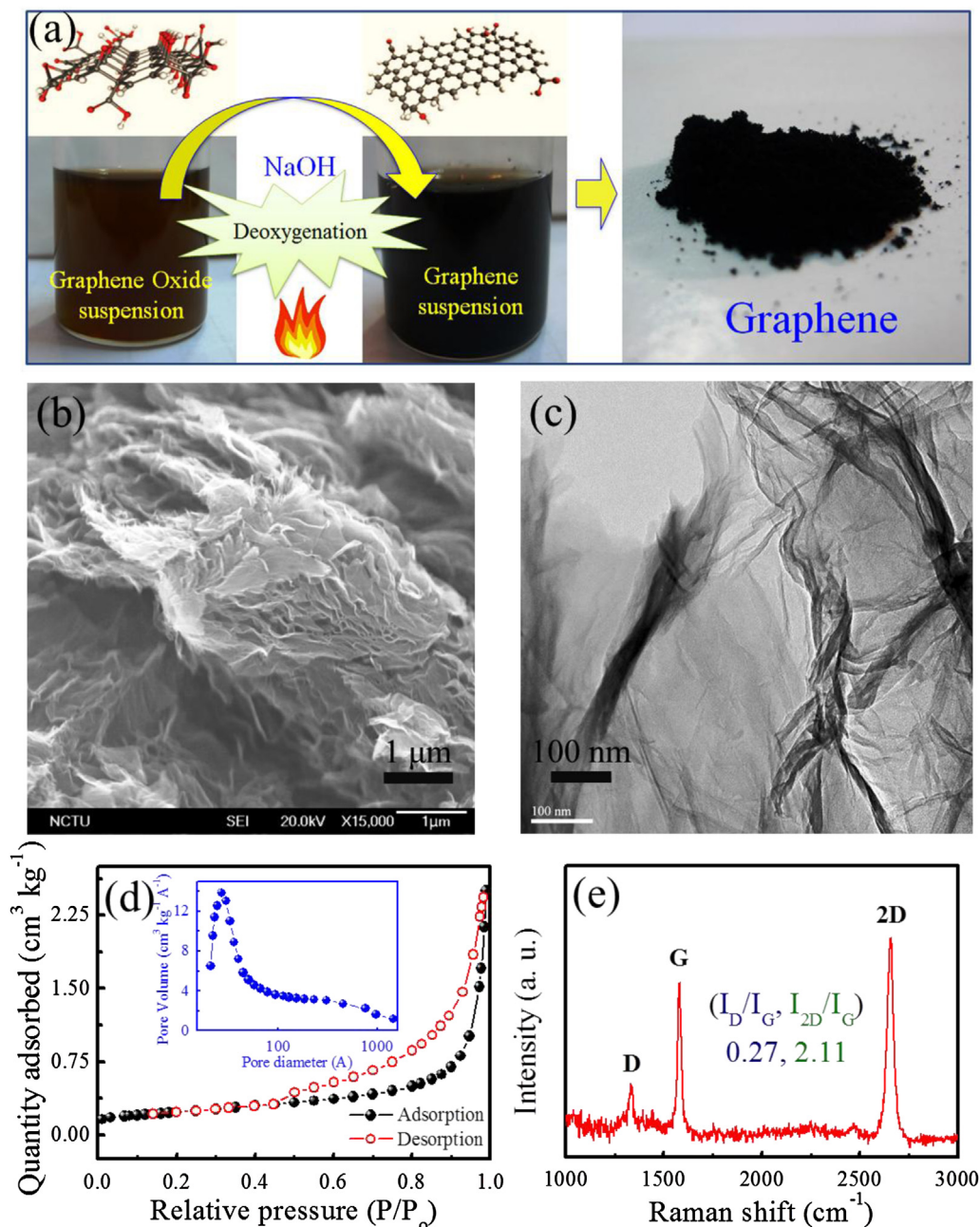
Fig. 1. (Color online) (a) Images of the suspension before and after the deoxygenation of exfoliated graphene oxide under alkaline (NaOH) conditions, and final black product (graphene), (b) SEM image, (c) TEM image, (d) N_2 adsorption−desorption isotherm, and (e) Raman analysis of the as-synthesized graphene.

network structure formation can serve as fast electronic and ionic conducting channels. Detailed observations of the surface morphologies are confirmed by TEM. The flake-like MnO_2 is well deposited on the GMC matrix surface, as shown in Fig. 2c. EDS spectrum corresponding to the marked region indicates that the coating is only composed of two elements, Mn and O, as shown in inset of Fig. 2c. Interestingly, the appearance of K peaks in the sample indicates K^+ co-existing in the MnO_2 matrix, arising from the precursor, $KMnO_4$, which always happens during the synthesis of MnO_2 [30].

The selected area electron diffraction pattern (SAED) of GMC + C nanocomposites is shown in the inset of Fig. 2c. SAED pattern exhibits six-fold hexagonal symmetry related to the basal plane of graphene, corresponding to diffraction patterns of (100) and (110).

It indicates successful restoration of the graphite structure in the reduced graphene oxide [31]. In addition, the diffraction rings can be indexed to the birnessite-type (002), (200), (112) crystal planes of MnO_2 nanosheets (JCPDS 43-1456). Continuous ring at SAED pattern also confirms their nanocrystalline nature.

XRD patterns of GC and GMC + C nanocomposites are depicted in Fig. 2d, indicating that the GC and GMC + C nanocomposites both exhibit the major peak at 2θ around 26.5° corresponding to the C (002) plane. This peak is common to both CNTs and graphene [32]. Moreover, the two weak characteristic peaks of GMC + C nanocomposites at 12.3° (001) and 24.9° (002) can be indexed to the characteristic reflections of birnessite-type MnO_2 phase. This result corroborates with the SAED results. However, broad diffraction peaks demonstrate that flake-like MnO_2 exhibits a poorly
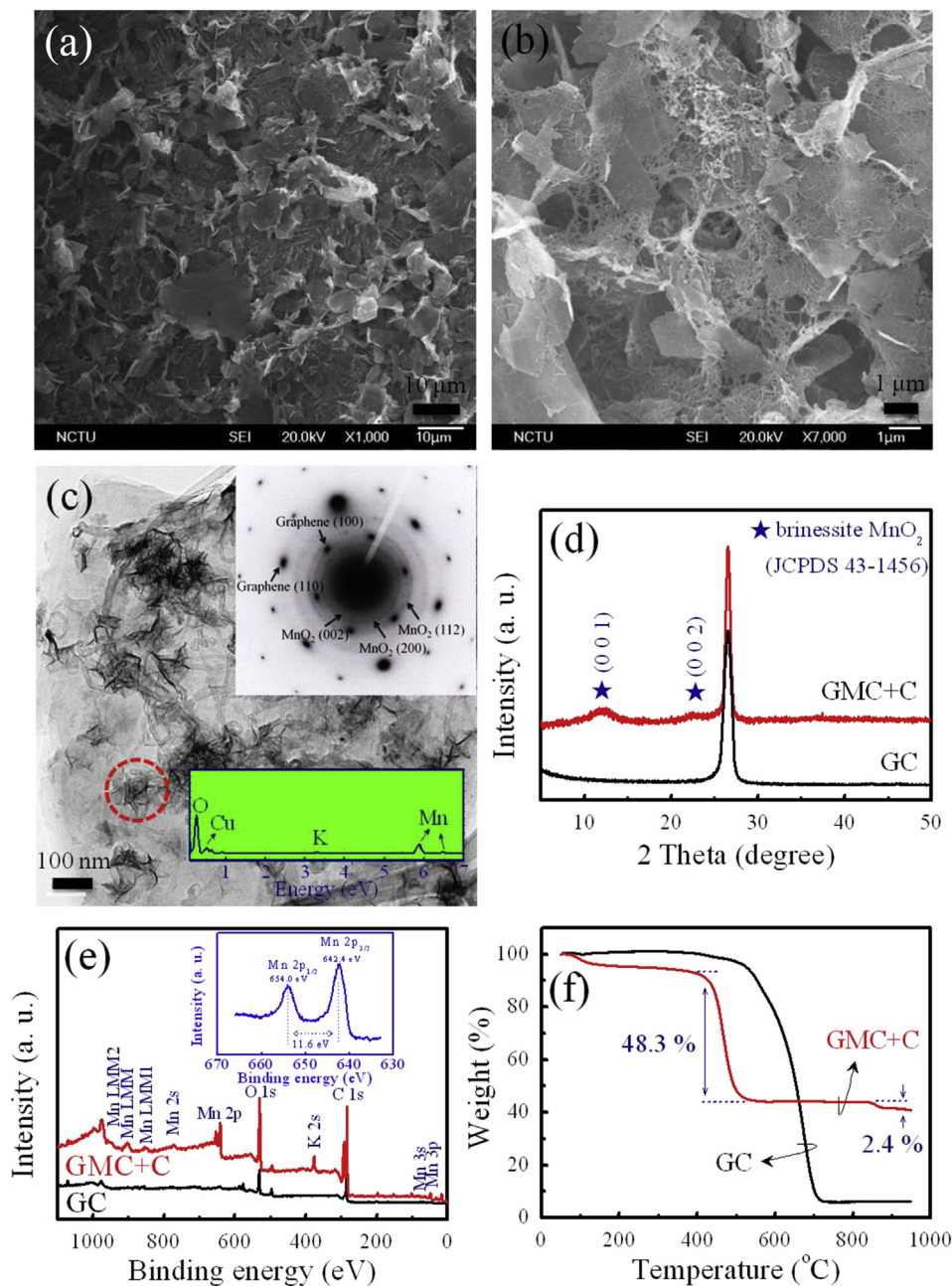
Fig. 2. (Color online) (a) SEM image of the deigned GC nanocomposite, (b) SEM image and (c) TEM image (the inset is corresponding selected area electron diffraction pattern and EDS spectrum of selected part) of the deigned GMC + C nanocomposite; (d) XRD, (e) wide XPS survey spectra (the inset is Mn 2p spectra of GMC + C nanocomposite), and (f) TGA curve of the designed GC (lower line) and GMC + C nanocomposite (upper line).

crystallized structure. The superior pseudocapacitive performance was obtained for MnO_2-based electrode containing higher amount of poorly crystallized birnessite phase [33,34]. Poorly crystallized birnessite phase has large interlayer distance and surface area-to-volume ratio, as a result pseudocapacitance is improved due to proton and cation of the electrolytes are easily inserted into the matrix.

Detailed surface chemical composition of GC and GMC + C nanocomposites is further analyzed by XPS, as shown in Fig. 2e. A scanning spectrum of the GC nanocomposites shows the presence of C 1s and O 1s signal. Compared with GC, Mn species is observed in the XPS wide spectrum of GMC + C, indicating the evidence of MnO_2 deposition on the porous network surface. In addition, the small amount of K 2s peak corresponds to $KMnO_4$, which is in

agreement with EDS result. To further investigate the oxidation state of Mn and confirm the composition, the Mn 2p spectra are individually shown in the inset of Fig. 2e. The XPS spectra are almost symmetrical, peaks of Mn $2p_{3/2}$ at 642.4 eV and Mn $2p_{1/2}$ at 654.0 eV, with a spin-energy separation of 11.6 eV, which are in good agreement with the previous reports of MnO_2 [35,36].

In order to understand the loading amount of MnO_2 on the matrix, the TGA curve was measured and used to determine the weight percentage of MnO_2 in the as-synthesized GMC + C nano-composites. Data were recorded in air at a ramp rate of 3 °C min^{-1} from 50 to 950 °C. Based on the TGA curve of GMC + C nano-composites, as shown in Fig. 2f, the weight loss of adsorbed and lattice water is about 6.9% between 50 and 390 °C. The additional 48.3% weight loss between 390 and 550 °C corresponds to the

removal of graphene/CNTs hybrid material. Furthermore, the final weight loss approximately 2.4% between 860 and 910 °C is associated with the conversion of MnO_2 to Mn_3O_4 [37].

In addition, TGA result of GC nanocomposites shows 96% loss (almost total weight) between 450 and 750 °C, which is attributed to the oxidation of the graphene/CNTs in air [24]. Thus, the actual percentages of MnO_2 and graphene/CNTs hybrid material matrix in the initial GMC + C nanocomposites are 40.8% and 48.3%, respectively.

The CV, CC, and CA measurements were employed to evaluate the pseudocapacitive behavior of GMC + C nanocomposites. Fig. 3a illustrates the typical CV curves of the GMC + C nanocomposite electrode in neutral aqueous electrolyte (0.1 M Na_2SO_4) at 25 °C in the potential range of $0 < E_{SCE} < 0.8$ V vs. SCE with different scan rate. All the CV curves appear almost a near-ideal symmetric rectangular profile and a rapid current response to a voltage reversal at each end potential even at a high scan rate of 500 mV s^{-1}. According to Eq. (1), the mean calculated specific capacitances are 860, 697, 634, 572, and 529 F g^{-1} as a function of different scan rates of 5, 50, 100, 300, and 500 mV s^{-1} respectively. It is shown that the specific capacitance decreases with increasing scan rate, as shown in inset of Fig. 3a, up to 61.5% specific capacitance can be retained when the scan rate increases 100 times from 5 to 500 mV s^{-1}. These results show excellent power capability of the designed GMC + C hybrid electrode.

In comparison with the CV results, the linear charge/discharge behavior is observed of GMC + C electrode in neutral aqueous electrolyte (0.1 M Na_2SO_4) at 25 °C in the range of $0 < E_{SCE} < 0.8$ V at various current densities, as shown in Fig. 3b. All these CC curves are very symmetric, and the charge/discharge duration decreases with an increase of current density. In addition, the slope of every

curve is potentially independent with a constant value; IR drops of all curves are dependent on various current densities from 1 to 10 A g^{-1}. According to Eq. (2), the specific capacitance of GMC + C electrode at current densities of 1, 2, 3.5, 5 and 10 A g^{-1} can be calculated as 964, 867, 746, 697, and 644 F g^{-1}, respectively. About 67% of specific capacitance is retained when the charge/discharge rate changes from 1 to 10 A g^{-1}. In addition, GMC + C electrode exhibits low resistance even at high current densities. The relationship is plotted in the inset of Fig. 3b.

To further understand the correlation between the mobilities of ions and electrons, CA experiment was used to measure the diffusion coefficient D. The D is calculated using following the Cottrell equation:

$$i_t = \frac{nFAC_0 D^{1/2}}{\pi^{1/2} t^{1/2}} \tag{3}$$

where n is stoichiometric number of electrons involved in the reaction; F, Faraday's constant (96,485 C mol^{-1}); A, area of the electrode surface (cm^2); C_0, is the concentration of electroactive species (mol cm^{-3}); and D, the diffusion coefficient (cm^2 s^{-1}). A Cottrell plot of the current, i vs. 1/square root of time, $t^{-1/2}$ transformed the data into a linear relationship whose slope is $nFAC_0 D^{1/2}\pi^{-1/2}$ [38]. The Cottrell plot of i vs. 1/sqrt(T) is obtained and a typical representation is made in Fig. 3c. Using the values of the forward and reverse slopes in Eq. (3), the calculated values of D for intercalation and deintercalation of Na$^+$ into/from the GMC + C nanocomposite in 0.1 M Na_2SO_4 are 6.34×10^{-7} cm^2 s^{-1} and 8.86×10^{-7} cm^2 s^{-1}, respectively, which are significantly better than those reported in previous works [39,40].
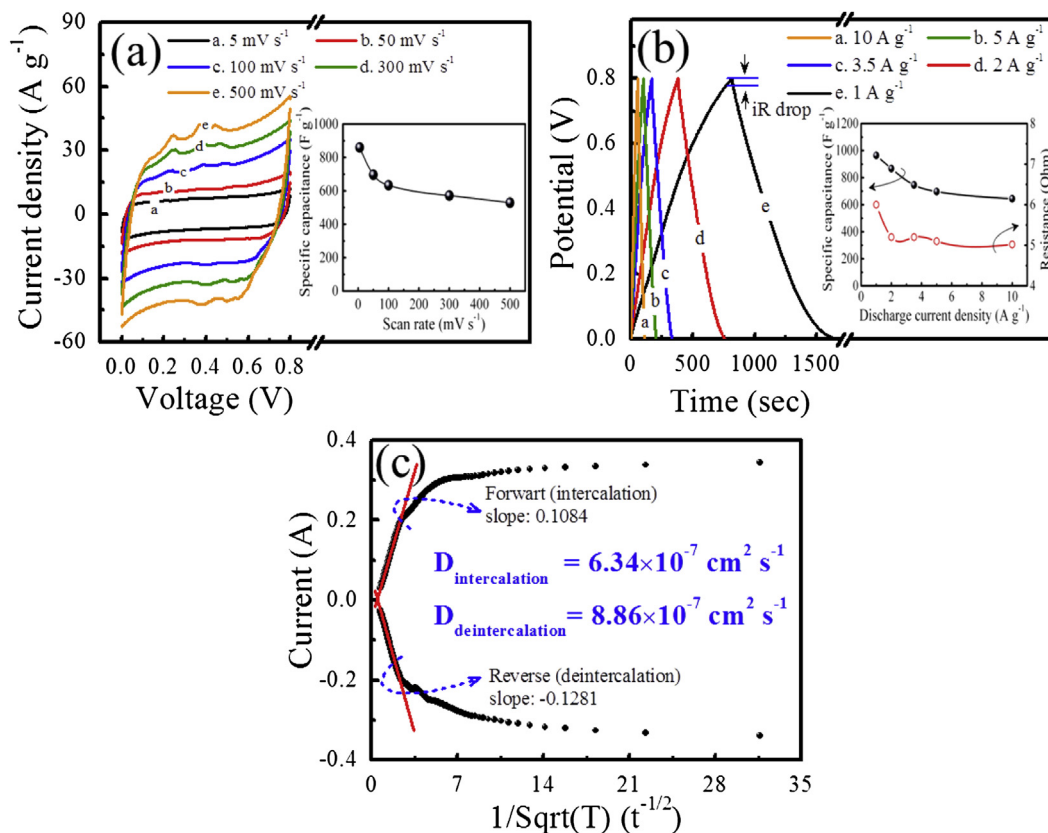

Fig. 3. (Color online) (a) The CV curves in 0.1 M Na_2SO_4 at scan rates of 5, 50, 100, 300 and 500 mV s^{-1} (the inset is the summary plot of specific capacitance from CV results), (b) the CC curves in 0.1 M Na_2SO_4 at current densities of 1, 2, 3.5, 5, and 10 A g^{-1} (the inset is the summary plot of specific capacitance from CC results), and (c) Cottrell plot for the CA analysis of GMC + C nanocomposite electrode at +2 V potential step.

From the above mentioned data, to enhance pseudocapacitive performance it is expected to use GMC + C hybrid porous structure, leading to that the electrolyte can flood into pores of its structure and its inner surface is suitable for ion diffusion. Moreover, CNTs plays a critical role in promoting the performance by acting as a spacer to prevent the re-stacking of individual MnO2/graphene/CNTs nanocomposite sheets.

In general, asymmetric pseudocapacitor that incorporates different materials for both anode and cathode electrodes promises a wider operating voltage and thus achieves higher energy density. One electrode is based on the high specific capacitance of the redox reaction character, and the other one is mostly based on the fast ion transport property of the electric double-layer storage. At this point, we assemble asymmetric pseudocapacitor using GMC + C nanocomposite as cathode and GC nanocomposite as anode in aqueous electrolyte (0.1 M Na$_2$SO$_4$), as shown in Fig. 4a. To further

evaluate the electrochemical potential window and chemical stability of GMC + C and GC nanocomposites, we performed CV measurements on the two-electrode materials using a three-electrode cell configuration before evaluating the asymmetric pseudocapacitor.

Fig. 4b shows the different stable potential windows of GMC + C and GC electrodes, indicates that both CV curves exhibit a nearly rectangular shape demonstrating an ideal capacitive behavior for both electrodes. The stable potential window is between −0.9 and 0 V for GC and between 0 and 0.9 V for GMC + C. The specific capacitances of the GC and GMC + C are 106 and 521 F g^{-1} at a scan rate of 25 mV s^{-1} respectively. In order to find the optimal cell voltage in asymmetric pseudocapacitor, a mass balance between the two electrodes is required to consider. Consequently, the mass ratio of anode electrode (GC) to cathode electrode (GMC + C) is decided according to the well-known charge balance theory
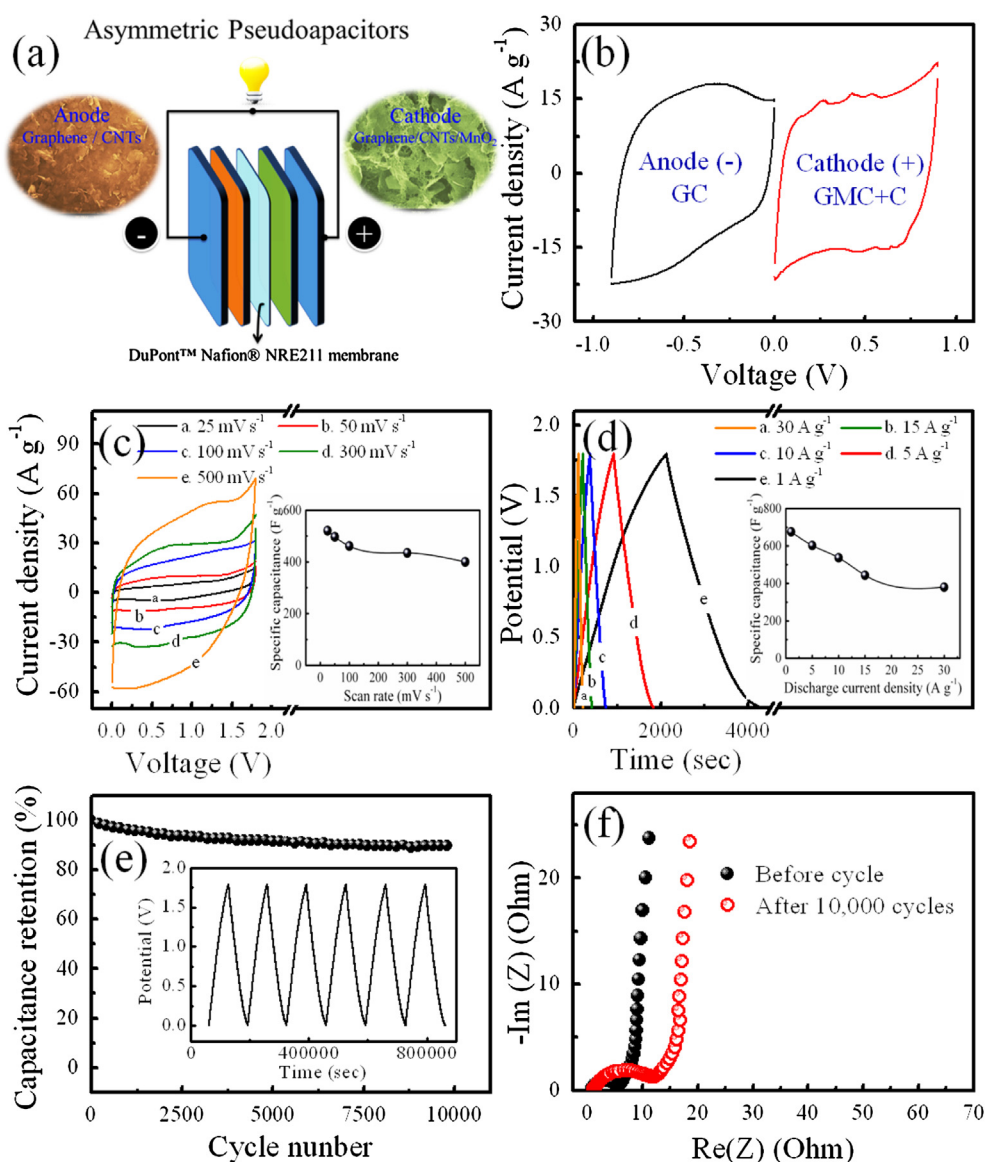

Fig. 4. (Color online) (a) Schematic illustration of the fabricated asymmetric pseudocapacitor configuration based on GMC + C as cathode and GC as anode in a neutral aqueous Na$_2$SO$_4$ electrolyte, (b) comparative CV curves of GMC + C and GC nanocomposites electrodes performed in a three-electrode cell in 0.1 M Na$_2$SO$_4$ aqueous solution at a scan rate of 25 mV s^{-1}, (c) the CV curves in 0.1 M Na$_2$SO$_4$ at scan rates of 25, 50, 100, 300 and 500 mV s^{-1} (the inset is the summary plot of specific capacitance from CV results), (e) the CC curves in 0.1 M Na$_2$SO$_4$ at current density of 1, 5, 10, 15, and 30 A g^{-1} (the inset is the summary plot of specific capacitance from CC results), (e) the cycling stability of the deigned asymmetric pseudocapacitor at a constant charge/discharge current density of 1 A g^{-1} (the inset is the charge/discharge curves of the last 6 cycles), and (f) Nyquist plot of GMC + C// GC asymmetric pseudocapacitor recorded before and after 10,000 cycles.

$(q^+ = q^-)$. In this relationship, the charge stored by each electrode usually depends on the specific capacitance (C), the potential window (ΔE) and the mass of active material (m), as shown in the following equation:

$$q = C \times \Delta E \times m \tag{4}$$

and in order to get $q^+ = q^-$, the mass balancing is calculated by the following equation:

$$\frac{m^+}{m^-} = \frac{C^- \times \Delta E^-}{C^+ \times \Delta E^+} \tag{5}$$

Based on the specific capacitance values and potential windows of GMC + C and GC electrodes, the asymmetric system voltage can be expressed as the sum of the potential range of GMC + C and GC. Consequently, it can be extended up to 1.8 V in 0.1 M aqueous Na$_2$SO$_4$ solution for the asymmetric pseudocapacitor of GMC + C// GC with the optimal mass ratio between the two electrodes fixed to $m^+_{GMC+C}/m^-_{GC} = 0.2$.

Fig. 4c describes the typical CV curves of optimized asymmetric pseudocapacitor measured at various scan rates between 0 and 1.8 V in 0.1 M Na$_2$SO$_4$ aqueous electrolyte. Generally, all the CV curves exhibit a quasi-rectangular shape and the total current increases with increasing scan rate. It is worthy to mention, with the increase of scan rates up to 500 mV s^{-1}, there are no distortion of CV curve is observed, indicating fast charge–discharge properties of the asymmetric device. However, it should pay an attention here that the specific capacitance is calculated on the basis of the total mass of active materials on two electrodes in the asymmetric pseudocapacitor, rather than on a single electrode. According to Eq. (1), the mean calculated specific capacitances are 521, 497, 462, 435, and 400 F g^{-1} as a function of different scan rates of 25, 50, 100, 300, and 500 mV s^{-1} respectively. It is clearly shown that the specific capacitance gradually decreases with increasing scan rate, as indicated in the inset of Fig. 4c, which is attributed to low utilization of active materials at higher scan rates [41]. However, the actual calculations based on a single electrode yield much higher values (1.5 times higher than two-electrode configurations); such approach should not be used to predict the asymmetrical configuration's performance [16,24].

In order to further evaluate the performance of asymmetrical pseudocapacitor, linear charge/discharge testing was also performed with different current densities with a voltage window of 1.8 V and the result is shown in Fig. 4d. The charge/discharge curves exhibit near symmetric triangular shapes and small equivalent series resistance, indicating good charge storage properties. According to Eq. (2), the mean calculated specific capacitances are 676, 603, 537, 444, and 380 F g^{-1} as a function of different current density of 1, 5, 10, 15, and 30 A g^{-1}, respectively. Even when the discharge current is enhanced 30 times, from 1 to 30 A g^{-1}, the specific capacitance still retains approximately 56% of its initial capacitance at a high current density. This result is plotted in the inset of Fig. 4d, corresponding to the behavior of ideal capacitors, which is agreed well with CV results.

Fig. 4e displays the cycling stability of the GMC + C//GC asymmetric pseudocapacitor at a constant charge/discharge current density of 1 A g^{-1}. It is indicated that the capacitance can achieve as high as 602 F g^{-1} retaining 89.0% of its initial capacitance after 10,000 continuous charge/discharge cycles, which demonstrates an excellent cycling performance. In addition, the last 6 cycles still exhibit a highly symmetric charge/discharge characteristic further proving the long period durability, as shown in inset of Fig. 4e.

Electrochemical impedance spectroscopy studies were conducted within the frequency range of 0.1 Hz–100 KHz at an open circuit voltage with AC amplitude of 5 mV. Fig. 4f shows the Nyquist plots of the EIS spectra for asymmetric pseudocapacitor before and after testing for 10,000 cycles, respectively. Both impedance spectra shown in this figure clearly depict the semi-circle type at the end of the Warburg-type line.

Upon long-term cycling, the EIS shows subtle changes. Firstly, the internal resistances after 10,000 cycles increased from 0.8 to 1.0 Ω at the high-frequency intercept of the real axis, suggesting that the electron conductivity of the GMC + C//GC configuration shows only a slight decline tendency. Secondly, the charge transfer resistances are evaluated from the diameter of the semi-circle, increasing from 6.1 to 13.8 Ω after long-term cycling, which imply that the electrolyte penetration and ion diffusion in the host materials are slightly reduced. In addition, the EIS spectra show almost vertical line at the low frequency region, and no any obvious change after long-term cycling, indicating that it still remain a low ion transport resistance in the pore structure of the nanocomposite. Importantly, even after 10,000 cycles, the internal resistance, charge transfer resistance, and Warburg impedance in the porous structure of the GMC + C//GC configuration still remain low; demonstrating that our designed asymmetric pseudocapacitors have a high pseudocapacitive performance and excellent cycling stability.

Furthermore, power density (P) and energy density (E) both are generally used as important parameters of asymmetric pseudocapacitor which evaluate its operational performance/efficiency. On the basis of the charge/discharge test results, the power density and energy density are calculated by using the following equations [42]:

$$E = \frac{C \times \Delta V^2}{2} \times \frac{1000}{3600} \left(\text{Energy Density/Wh kg}^{-1} \right) \tag{6}$$

$$P = \frac{\Delta V^2}{4 \times \text{ESR} \times M_{ac}} \left(\text{Power Density/kW kg}^{-1} \right) \tag{7}$$

where V is the applied voltage, ESR the internal resistance, M_{ac} the total mass of active electrode materials used in asymmetric pseudocapacitors, and C is the measured total specific capacitance of asymmetric pseudocapacitors.

The internal resistance is determined from the voltage drop at the beginning of each discharge

$$\text{ESR} = \frac{iR_{drop}}{2 \times I} \left(\text{Equivalent Series Resistance}/\Omega \right) \tag{8}$$

iR_{drop} is the voltage drop between the first two points from its top cut-off. I the current applied.

These results are summarized as the Ragone plot in Fig. 5. It is shown that the energy densities decrease slowly with the increasing of power densities. The maximum energy density of 304.1 Wh kg^{-1} (for a power density of 19.9 kW kg^{-1}) and the highest power density of 242.1 kW kg^{-1} (for an energy density of 171.2 Wh kg^{-1}) are achieved using our designed GMC + C//GC asymmetric pseudocapacitors at an operation voltage of 1.8 V. This energy density value is indeed much higher than those energy density values of MnO$_2$-based asymmetric pseudocapacitors in aqueous electrolytes reported previously, including graphene/MnO$_2$//activated carbon nanofibers (51.1 Wh kg^{-1} at 198 kW kg^{-1}) [12], graphite oxide/MnO$_2$//graphite oxide (24.3 Wh kg^{-1} at 24.5 kW kg^{-1}) [13], MnO$_2$//graphene (23.2 Wh kg^{-1} at 1 kW kg^{-1}) [14], graphene/MnO$_2$//graphene/Ag (7.5 Wh kg^{-1} at 90.3 kW kg^{-1}) [15], graphene/MnO$_2$/CNTs//activated carbon/CNTs (24 Wh kg^{-1} at 7.8 kW kg^{-1}) [16], MnO$_2$/CNTs//CNTs (73.6 Wh kg^{-1} at 14.6 kW kg^{-1}) [17].

Finally, we also found that the designed GMC + C//GC asymmetric pseudocapacitors can light a red emitting diode, as shown in
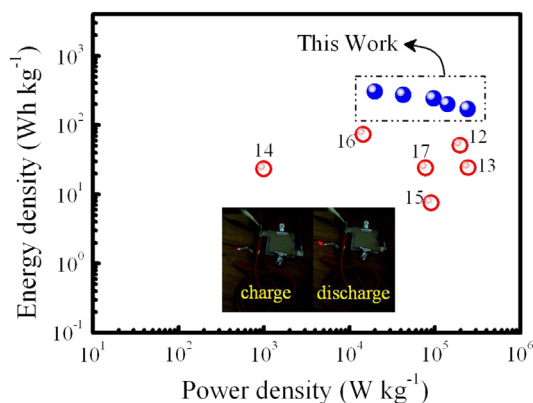
Fig. 5. Ragone plots of GMC + C//GC asymmetric pseudocapacitors compared with other MnO$_2$-based asymmetric configurations with an aqueous electrolyte in previous literature (the inset is the photograph of GMC + C//GC cell lighting up a red emitting diode).

the inset of Fig. 5, demonstrating its practical application in the energy storage/conversion system.

4. Conclusions

In summary, we fabricated novel hybrid nanocomposite thin-film electrodes with high surface area and interconnected pore networks via EPD. The GMC + C nanocomposite electrode displays excellent electrochemical performance with respect to the maximal specific capacitance of 964 F g^{-1} (at the current density of 1 A g^{-1}), remarkable rate capability (with the residual capacitance of 529 F g^{-1} at the high scan rate of 500 mV s^{-1}), and fast Na$^+$ diffusion (intercalation value: 6.34×10^{-7} cm^2 s^{-1}, deintercalation value: 8.86×10^{-7} cm^2 s^{-1}). It indicates that the designed nanocomposites can provide a synergistic improvement on electrochemical performance as well as offering uninterrupted electron-conducting and ion-diffusing pathways. Furthermore, the asymmetric pseudocapacitors assembled using GMC + C as the cathode, GC as the anode, and 0.1 M Na$_2$SO$_4$ as the aqueous electrolyte, exhibiting a record high energy density of 304 Wh kg^{-1} and retaining 56.2% of its initial specific energy density at the power density up to 242 kW kg^{-1}. In addition, the asymmetric cell configuration also possesses excellent cycling stability with 89% of the specific capacitance maintained after 10,000 cycle tests. These results indicate that our designed asymmetric pseudocapacitors are appropriate for practical applications.

Acknowledgments

References

[1] M. Yu, T. Zhai, X. Lu, X. Chen, S. Xie, W. Li, C. Liang, W. Zhao, L. Zhang, Y. Tong, J. Power Sourc. 239 (2013) 64.
[2] Y. Gao, Y.S. Zhou, M. Qian, H.M. Li, J. Redepenning, L.S. Fan, X.N. He, W. Xiong, X. Huang, M. Majhouri-Samani, L. Jiangd, Y.F. Lu, RSC Adv. 3 (2013) 20613.
[3] H. Jiang, P.S. Lee, C. Li, Energy Environ. Sci. 6 (2013) 41.
[4] I.E. Rauda, V. Augustyn, B. Dunn, S.H. Tolbert, Accounts Chem. Res. 46 (2013) 1113.
[5] X. Lang, A. Hirata, T. Fujita, M. Chen, Nat. Nanotechnol. 6 (2011) 232.
[6] R. Gupta, N.K. Sharma, P. Tiwari, A. Gupta, N. Nigam, A. Gupta, Int. J. Eng. Sci. Technol. 3 (2011) 289.
[7] H. Zhong, F. Xu, Z. Li, R. Fu, D. Wu, Nanoscale 5 (2013) 4678.
[8] H.Q. Wang, Z.S. Li, Y.G. Huang, Q.Y. Li, X.Y. Wang, J. Mater. Chem. 20 (2010) 3883.
[9] Q. Cheng, J. Tang, J. Ma, H. Zhang, N. Shinya, L.C. Qinc, Phys. Chem. Chem. Phys. 13 (2011) 17615.
[10] S. Vaquero, J. Palma, M. Anderson, R. Marcilla, Int. J. Electrochem. Sci. 8 (2013) 10293.
[11] G. Yu, X. Xie, L. Pand, Z. Baod, Y. Cui, Nano Energy 2 (2013) 213.
[12] Z. Fan, J. Yan, T. Wei, L. Zhi, G. Ning, T. Li, F. Wei, Adv. Funct. Mater. 21 (2011) 2366.
[13] X. Zhao, L. Zhang, S. Murali, M.D. Stoller, Q. Zhang, Y. Zhu, R.S. Ruoff, ACS Nano 6 (2012) 5404.
[14] H. Gao, F. Xiao, C.B. Ching, H. Duan, ACS Appl. Mater. Interfaces 4 (2012) 2801.
[15] Y. Shao, H. Wang, Q. Zhang, Y. Li, J. Mater. Chem. C 1 (2013) 1245.
[16] Y. Cheng, H. Zhang, S. Lu, C.V. Varanasiad, J. Liu, Nanoscale 5 (2013) 1067.
[17] J. Shen, A. Liu, Y. Tu, H. Wang, R. Jiang, J. Ouyang, Y. Chen, Electrochim. Acta 78 (2012) 122.
[18] F. Wang, S. Xiao, Y. Hou, C. Hu, L. Liu, Y. Wu, RSC Adv. 3 (2013) 13059.
[19] M.R. Lukatskaya, O. Mashtalir, C.E. Ren, Y. Dall'Agnese, P. Rozier, P.L. Taberna, M. Naguib, P. Simon, M.W. Barsoum, Y. Gogotsi, Science 341 (2013) 1502.
[20] H. Wang, Y. Liang, T. Mirfakhrai, Z. Chen, H.S. Casalongue, H. Dai, Nano Res. 4 (2011) 729.
[21] H. Gao, F. Xiao, C.B. Ching, H. Duan, ACS Appl. Mater. Interfaces 4 (2012) 7020.
[22] C.J. Hung, J.H. Hung, P. Lin, T.Y. Tseng, J. Electrochem. Soc. 158 (2011) A942.
[23] C.J. Hung, P. Lin, T.Y. Tseng, J. Power Sourc. 243 (2013) 594.
[24] R.B. Rakhi, W. Chen, D. Cha, H.N. Alshareef, Adv. Energy Mater. 2 (2012) 381.
[25] S. Gurunathan, J.W. Han, V. Eppakayala, A.A. Dayem, D.N. Kwon, J.H. Kim, Nanoscale Res. Lett. 8 (2013) 393.
[26] S. Pei, H.M. Cheng, Carbon 50 (2012) 3210.
[27] B.Z. Jang, A. Zhamu, J. Mater. Sci. 43 (2008) 5092.
[28] D.W. Wang, F. Li, Z.S. Wu, W. Ren, H.M. Cheng, Electrochem. Commun. 11 (2009) 1729.
[29] Z. Ni, Y. Wang, T. Yu, Z. Shen, Nano Res. 1 (2008) 273.
[30] H.Q. Wang, G.F. Yang, Q.Y. Li, X.X. Zhong, F.P. Wang, Z.S. Li, Y.H. Li, New J. Chem. 35 (2011) 469.
[31] A.K. Mondal, B. Wang, D. Su, Y. Wang, S. Chen, X. Zhang, G. Wang, Mater. Chem. Phys. 143 (2014) 740.
[32] S.S.J. Aravind, V. Eswaraiah, S. Ramaprabhu, J. Mater. Chem. 21 (2011) 15179.
[33] H.Y. Chu, Q.Y. Lai, L. Wang, J.F. Lu, Y. Zhao, Ionics 16 (2010) 233.
[34] O. Ghodbane, J.L. Pascal, F. Favier, ACS Appl. Mater. Interfaces 1 (2009) 1130.
[35] J. Liu, J. Jiang, M. Bosmanc, H.J. Fan, J. Mater. Chem. 22 (2012) 2419.
[36] J. Zeng, J.R. Nair, C. Francia, S. Bodoardo, N. Penazzi, Int. J. Electrochem. Sci. 8 (2013) 3912.
[37] J. Li, N. Wang, Y. Zhao, Y. Ding, L. Guan, Electrochem. Commun. 13 (2011) 698.
[38] M.F. Nazarudin, Z. Zainal, W.T. Tan, I. Hamadneh, E.F. Kadri, Int. J. Electrochem. Sci. 7 (2012) 2965.
[39] M.N. Patel, X. Wang, B. Wilson, D.A. Ferrer, S. Dai, K.J. Stevenson, K.P. Johnston, J. Mater. Chem. 20 (2010) 390.
[40] M.N. Patel, X. Wang, D.A. Slanac, D.A. Ferrer, S. Dai, K.P. Johnston, K.J. Stevenson, J. Mater. Chem. 22 (2012) 3160.
[41] K. Karthikeyan, S. Amaresh, K.J. Kim, S.H. Kim, K.Y. Chung, B.W. Cho, Y.S. Lee, Nanoscale 5 (2013) 5958.
[42] H. Yu, J. Wu, L. Fan, K. Xu, X. Zhong, Y. Lin, J. Lin, Electrochim. Acta 56 (2011) 6881.